PERGAMON

International Journal of Heat and Mass Transfer 44 (2001) 4667–4677

International Journal of HEAT and MASS TRANSFER

www.elsevier.com/locate/ijhmt

In-flight oxidation of composite powder particles during thermal spraying

A.M. Ahmed [a], R.H. Rangel [a,*], V.V. Sobolev [b], J.M. Guilemany [b]

[a] Department of Mechanical and Aerospace Engineering, University of California, Irvine, CA 92697-3975, USA

[b] CPT Thermal Spray Center, Materials Engineering Department, Enginyería Química i Metallúrgia, Universitat de Barcelona, Marti i Franqués, 1.E-08028 Barcelona, Spain

Received 1 September 2000; received in revised form 28 February 2001

Abstract

This paper presents a mathematical model of the in-flight thermal behavior and oxidation of powder particles during thermal spray deposition. In particular, stainless steel and Cr_3C_2–NiCr particles are investigated. The in-flight model accounts for the acceleration and deceleration of the particles during flight under variable fluid velocity, while the thermal model takes into account heating, melting, cooling and possible solidification as the particle travels towards the substrate. A finite difference method is used to solve the thermal energy conservation equation of the particles. The model includes non-equilibrium calculations of the phase change phenomena in the liquid–solid (mushy) zone and dissolution of the ceramic reinforcement in the composite particles. The growth of the oxide layer at the particle surface is represented by a modified boundary condition, which includes finite-rate oxidation. The results obtained give the interrelations between various process parameters and the oxidation phenomenon.

1. Introduction

Thermal spray atomization and deposition is a micro-solidification and consolidation methodology that involves a large population of small droplets. These processes are characterized by high temperature and velocity changes. The presence of oxidizing agents in the atomization gas causes a chemical reaction that leads to the oxidation of the sprayed droplets. One of the most rapidly developing areas in thermal spray technology, since it was first developed in the early 1980s, is the high velocity oxy-fuel (HVOF) thermal spraying [1]. During HVOF, an internal combustion process rapidly heats and accelerates a metal powder to a high temperature and velocity as the particles are melted and deposited on a substrate. Understanding the thermal and mechanical behavior of the powder particles during the HVOF spray process is of interest in the pursuit of its improvement. Modeling of HVOF processes for a variety of powders has been considered by Sobolev and Guilemany [2], among others.

During thermal spraying, the excess oxygen in the combustion products reacts with the metal particles leading to their oxidation. The purpose of this paper is to present a mathematical model for the in-flight oxidation of stainless steel and ceramic powder particles. The dynamics of particle motion as well as particle heating, cooling and phase change are taken into account.

Available oxidation models for stainless steel are mainly presented in integral form where the oxide layer thickness is proportional to the elapsed time raised to some exponent, with the oxidation rate constant being temperature dependent (see [3,4]). These equations are derived from experimental data for stainless steel oxidation at temperatures below the melting point. As such, these models are not suitable for the prediction of oxide layer thickness for thermal spray processes. In fact, these equations produce a decrease in oxide layer thickness as the particle temperature decreases during cooling. Furthermore, there is no oxidation model for composite particles in thermal spraying.

* Corresponding author. Tel.: +1-949-824-4033; fax: +1-949-824-8585.

E-mail address: rhrangel@uci.edu (R.H. Rangel).

0017-9310/01/$ - see front matter
PII: S0017-9310(01)00093-X

Nomenclature

A	a constant defined in Eq. (10)
C_{drag}	drag coefficient
C_b	concentration in the surroundings of a Cr_3C_2 particle (mole/m^3)
c_d	concentration inside a Cr_3C_2 particle (mole/m^3)
c_ℓ	liquid concentration in a binary alloy (mole/m^3)
c_p	specific heat (J/kg K)
c_s	solid concentration in a binary alloy (mole/m^3)
c_w	concentration on the surface of a Cr_3C_2 particle (mole/m^3)
d	particle diameter(m)
g	acceleration of gravity (m/s^2)
ΔH_{ox}	heat of oxidation (J/kg)
h	convective heat transfer coefficient (W/m^2 K)
h_{sf}	heat of fusion (J/kg)
k	thermal conductivity (W/m K)
Nu	Nusselt number (hd/k_g)
r	radial coordinate (m)
R	particle radius (m)
R_c	Cr_3C_2 particle radius (m)
Re	Reynolds number ($\lvert V_p - V_g \rvert d\rho_g/\mu_g$)
t	time (s)
t_*	time at the onset of melting (s)
T	temperature (K)
T_k	the melting temperature of the solvent (K)
T_ℓ	liquidus temperature (K)
T_m	melting temperature (K)
T_s	solidus temperature (K)
U	overall heat transfer coefficient (W/m^2 K)
V	velocity (m/s)
X	particle position (m)
z	axial position (m)

Greek symbols

α	thermal diffusivity (m^2/s)
d	oxidation layer thickness (Å)
κ	partition coefficient ($\kappa = c_s/c_\ell$)
m	dynamic viscosity (kg/ms)
r	density (kg/m^3)

Subscripts

g	gas
ox	oxide, oxidation
p	particle
R	particle surface position

We present a model that can be used to predict the oxide volume fraction for stainless steel (Fig. 1(a)) and composite ceramic particles (Fig. 1(b)) in thermal spray deposition processes. The model is a modified version of an oxidation model that is based on the Mott–Cabrera theory for the oxidation of aluminum in thermal spraying [5]. The model constants are modified to fit the oxidation of stainless steel using available experimental data from the HVOF spray facility at the University of Barcelona. Delplanque et al. [6] have used a Mott–Cabrera model to study the oxidation of aluminum particles.

2. Analysis

The equation governing the thermal behavior of a binary alloy particle, under the conditions of spherical symmetry, can be written as

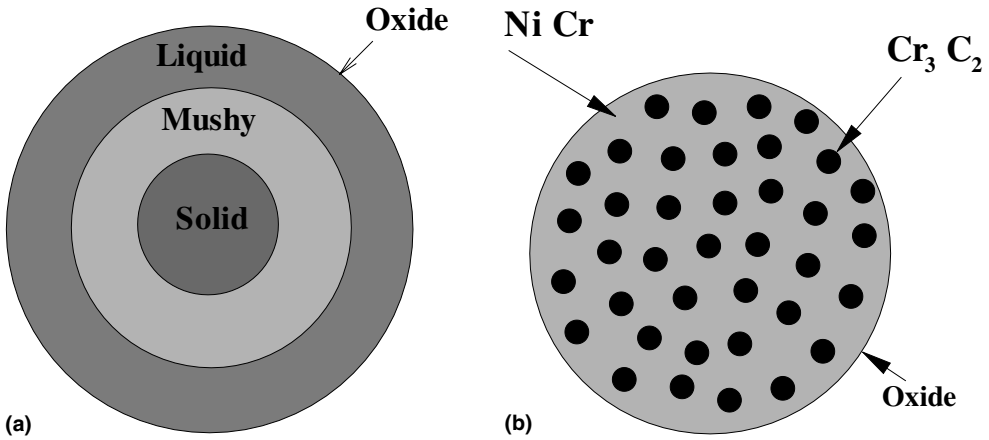

Fig. 1. Schematic of (a) stainless steel, (b) composite particle.

$$\rho c_p \frac{\partial T}{\partial t} = k\left(\frac{\partial^2 T}{\partial r^2} + \frac{2}{r}\frac{\partial T}{\partial r}\right) + h_{sf}\rho\frac{dx}{dt}, \quad (1)$$

where T is the temperature, t is the time, r is the radial distance from the particle center, x is the solid fraction per unit mass, ρ is the density, c_p is the specific heat and h_{sf} is the latent heat of fusion. If the region of the binary phase diagram where solidification is taking place, can be approximated by straight lines, as in the case of stainless steel using a carbon-equivalent C–Fe alloy model, Eq. (1) can be written as [2]:

$$\psi(T)\frac{\partial T}{\partial t} = \alpha\left(\frac{\partial^2 T}{\partial r^2} + \frac{2}{r}\frac{\partial T}{\partial r}\right), \quad (2)$$

where α is the thermal diffusivity and $\psi(T)$ is a function that takes the value of unity if T is less than the solidus temperature (T_s) or more than the liquidus temperature (T_ℓ), while, in the range $T_s \leqslant T \leqslant T_\ell$ is equal to

$$\psi(T) = 1 + \frac{h_s f (T_k - T_\ell)^{1/(1-\kappa)}}{c_p(1-\kappa)(T_k - T)^{(2-\kappa)/(1-\kappa)}}, \quad (3)$$

where T_k is the melting temperature of the primary element (the solvent) and κ is the partition coefficient. It is assumed that diffusion is infinitely fast (equilibrium) in the liquid phase but equal to zero in the solid phase [7]. For the case when the liquidus and solidus temperature curves in the phase diagram cannot be approximated as straight lines, the function $\psi(T)$, can be written as

$$\psi(T) = 1 + \frac{h_{sf}}{c_p(c_\ell - c_s)^2}\left(k_2(c_\ell - c_s) + (k_1 - k_2 T)\frac{\partial(c_\ell - c_s)}{\partial T}\right), \quad (4)$$

where c_ℓ is the liquid concentration in the binary phase diagram, c_s is the solid concentration and k_1, k_2 are constants in the equation that approximates segments of the binary phase diagram boundaries as straight lines. The boundary conditions for Eq. (2) are a symmetry condition at the center of the particle and a convective cooling condition at the surface:

$$\left.\frac{\partial T}{\partial r}\right|_{r=0} = 0, \quad \left. k\frac{\partial T}{\partial r}\right|_{r=R} = h(T_g - T_R), \quad (5)$$

where R is the particle radius, T_g is the cooling gas temperature, T_R is the particle surface temperature, k is the particle thermal conductivity and h is the convective heat transfer coefficient. The convective heat transfer coefficient can be expressed in terms of the Nusselt number, $Nu = hd/k_g$, where d is the particle diameter. In our calculations, we use the Ranz and Marshall [8] experimental correlation modified for variable properties [9]

$$Nu = \left(2 + 0.6 Re^{1/2} Pr^{1/3}\right)\left(\frac{\rho_g \mu_g}{\rho_w \mu_w}\right)^{0.6}, \quad (6)$$

where subscript g stands for a gas property at the surrounding gas temperature and subscript w stands for a gas property at the particle surface temperature. In addition to the boundary conditions, the initial particle temperature is specified. Except for the specific heat, which is assumed constant, temperature-dependent gas properties are used. The density, ρ, viscosity, μ, and thermal conductivity, k, of the gas are given by [10]:

$$\frac{\rho_g}{\rho_{g0}} = \frac{T_{g0}}{T_g}, \quad \frac{\mu_g}{\mu_{g0}} = \left(\frac{T_g}{T_{g0}}\right)^{0.72}, \quad \text{and} \quad \frac{k_g}{k_{g0}} = \left(\frac{T_g}{T_{g0}}\right)^{0.73}, \quad (7)$$

where $T_{g0} = 3023$ K, $\rho_{g0} = 0.136$ kg/m^3, $\mu_{g0} = 8.75 \times 10^{-5}$ kg/ms and $k_{g0} = 0.2037$ W/m K. The specific heat used in our calculations is 1658 J/kg K. The physical properties of the stainless steel and the components of the composite particle are shown in Table 1.

In the case of the composite (Cr_3C_2–NiCr) particles, the thermo-physical properties depend on the instantaneous composition, which varies due to Cr_3C_2 dissolution. The composite consists of a ceramic Cr_3C_2 reinforcement in a NiCr matrix as illustrated in Fig. 1(b). When the metal matrix melts, the Cr_3C_2 reinforcement dissolves into the NiCr matrix, resulting in a change in the volume fraction of both the Cr_3C_2 and the NiCr matrix. For simplicity, we assume that the reinforcement particles are spherical. If at any given instant, the concentration distribution for a single Cr_3C_2 reinforcement particle is as seen in Fig. 2, it can be shown analytically that the radius R_c of the Cr_3C_2 reinforcement particle decreases in time according to

$$R_c^2(t) = R_c^2(0) - \frac{2D(c_w - c_b)}{c_d}t, \quad (8)$$

where D is the diffusion coefficient, c_w is the Cr_3C_2 dissolved concentration in the liquid at the Cr_3C_2 particle surface, c_d is the Cr_3C_2 concentration inside the reinforcement particle (equal to 1) and c_b is the Cr_3C_2 dissolved concentration in the liquid matrix, far from the Cr_3C_2 particle. Starting from Eq. (8), we can derive an equation for the instantaneous Cr_3C_2 volume fraction ε_{CrC}, i.e., [11]:

$$\varepsilon_{CrC} = \varepsilon^0_{CrC}(1 - At)^{3/2}, \quad (9)$$

where ε^0_{CrC} is the initial Cr_3C_2 volume fraction and A is a constant given by

$$A = \frac{1}{t_*}\left[1 - \left(\frac{\varepsilon^f_{CrC}}{\varepsilon^0_{CrC}}\right)^{2/3}\right]. \quad (10)$$

The superscripts f and 0 stand, respectively, for the final and initial values of the Cr_3C_2 volume fraction, and t_* is the elapsed time at the onset of melting of the metal matrix. The value of A is determined from experimental

Table 1
Properties of stainless steel and the composite particle components. The Ni–Cr(1) matrix is composed of 25% Cr and 75% Ni and the Ni–Cr(2) matrix is composed of 65% Cr and 35% Ni

	ρ (kg/m^3)	c_p (J/kg K)	k (W/m K)	h_{sf} (J/kg)	T_m (°C)	T_ℓ (°C)	T_s (°C)	T_k (°C)
SS	8000	480	26	0.272×10^6		1400	1375	1534
Ni	8900	471	83	0.3×10^6	1453			
Cr	7190	460	67	0.27×10^6	1880			
Ni–Cr(1)	8473	468	79	0.29×10^6		1440	1400	1453
Ni–Cr(2)	7788	464	73	0.28×10^6		1520	1345	1880
Cr_3C_2	6600	300	95	–				

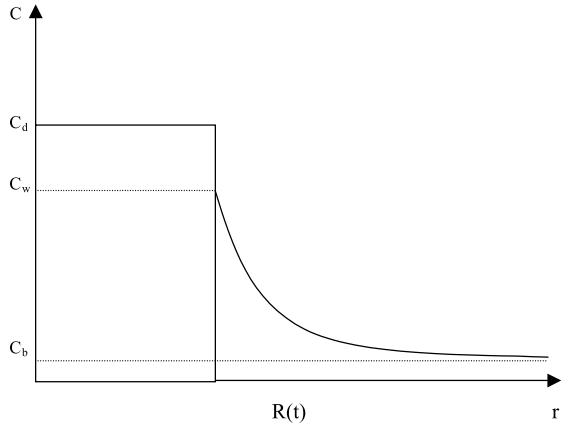

Fig. 2. Concentration distribution, in and around a single Cr_3C_2 sphere.

data for ε^0_{CrC} and ε^f_{CrC}. The values of the thermo-physical properties of the particle are determined from

$$\begin{aligned} k &= \varepsilon_{Ni}k_{Ni} + \varepsilon_{Cr}k_{Cr} + \varepsilon_{CrC}k_{CrC}, \\ \rho &= \varepsilon_{Ni}\rho_{Ni} + \varepsilon_{Cr}\rho_{Cr} + \varepsilon_{CrC}\rho_{CrC}, \\ c_p &= \varepsilon_{Ni}c_{p_{Ni}} + \varepsilon_{Cr}c_{p_{Cr}} + \varepsilon_{CrC}c_{p_{CrC}}, \end{aligned} \tag{11}$$

where ε_{Ni} and ε_{Cr} are the volume fractions of the Ni and Cr components, respectively, determined from

$$\frac{\varepsilon_{Ni}}{\varepsilon^0_{Ni}} = \frac{1-\varepsilon_{CrC}}{1-\varepsilon^0_{CrC}}, \quad \frac{\varepsilon_{Cr}}{\varepsilon^0_{Cr}} = \frac{1-\varepsilon_{CrC}}{1-\varepsilon^0_{CrC}} \tag{12}$$

with the superscript 0 denoting initial values.

3. Oxidation model

If the gas surrounding the particles during flight is not inert, a chemical reaction between the particle and the gas may take place. In particular, if the gas has enough oxygen concentration, oxidation of the particle surface occurs. Considering that the resulting oxidation layer is very thin, we assume that the heat released during oxidation is localized on the particle surface. Thus, the convective boundary condition (5) may be modified as

$$-k\left.\frac{\partial T}{\partial r}\right|_{r=R} + \rho\Delta H_{ox}\frac{d\delta}{dt} = \frac{T_R - T_g}{(\delta/k_{ox}) + (1/h)}, \tag{13}$$

where ΔH_{ox} is the heat released during oxidation, δ is the oxidation layer thickness and k_{ox} is the oxide layer conductivity. The rate of growth of the oxidation layer can be calculated from [5]

$$\frac{d\delta}{dt} = 2A_0 \exp\left(-\frac{Q}{k_b T_R}\right)\exp\left(\frac{K_0\sqrt{P_{O_2}}}{k_b T_R}\right), \tag{14}$$

where k_b is the Boltzmann constant and P_{O_2} is the O_2 partial pressure in Torr. In the case of stainless steel, the constants A_0 and Q could be evaluated, for example, from the experimental data for stainless steel 410 provided by McCullough et al. [3] and using the procedure outlined by Fehlner [12]. The experimental data are plotted as $1/\delta$ and $\ln(t/\delta^2)$ (δ in Å and t in s). A straight line is fitted to these data and the values of the slope m and intercept b are determined. These values are then used to determine $u(u = 2A_0 \exp(-Q/k_bT))$ for each value of T. Fig. 3 shows the plot of ln(u) versus $1/T$ and a linear fit that is used to determine the slope and intercept. The slope is used to determine Q and the intercept is used to determine A_0. This procedure results in the values $A_0 = 5.5 \times 10^4$ Å/s, $K_0 = 0.139$ eV/$\sqrt{\text{torr}}$, and $Q = 1.1$ eV. However, since these parameters are obtained from data for the oxidation of the solid phase, they may not be appropriate to predict oxidation of the liquid. Alternatively, the constants in Eq. (14) may be determined using available experimental data on final oxide volume fractions from four different runs with different oxygen concentrations and spraying distances [3]. The underlying assumption is that significant oxidation occurs only in-flight, with negligible oxidation on the substrate. Oxidation rates while on the substrate should be several orders of magnitude smaller than those during flight because the characteristic time on the substrate is of the order of μs, while it is of the order of ms during flight. Moreover, the oxidation rate of the solid phase is about three orders of magnitude smaller than that of the liquid phase. The known particle diameters and size distributions from the experiments are used in the calculations to determine the final oxide volume fraction. The optimum values of the constants A_0, Q and K_0 are determined when the root mean square difference between numerical and experimental data is minimal. For comparison, the values obtained in this way are: $A_0 = 5 \times 10^6$ Å/s, $Q = 1.5$ eV, and $K_0 = 0.149$ eV/$\sqrt{\text{torr}}$. The values obtained by Dai et al. [5] for the oxidation of aluminum are $A_0 = 2.5 \times 10^6$ Å/s, $Q = 1.6$ eV, and $K_0 = 0.139$ eV/$\sqrt{\text{torr}}$.

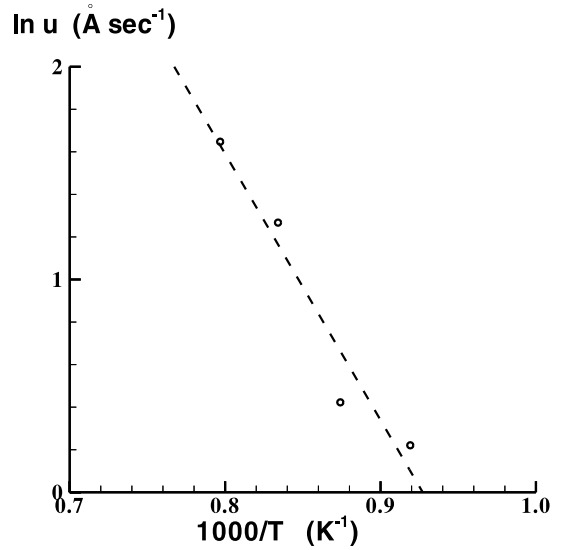

Fig. 3. Plot of $\ln(u)$ versus $1/T$ used in determining the oxidation equation constants Q and A_0.

The heat released during oxidation is calculated from the chemical reaction equations. The stainless steel used in our calculations is composed of 82.88% Fe, 0.12% C and 17% Cr. Since carbon content is very small, we consider only the oxidation of iron and chromium in our calculations. At high temperature the oxidation of iron takes place according to the following equation:

$$\mathrm{Fe} + \frac{1}{2}\mathrm{O_2} = \mathrm{FeO}. \tag{15}$$

At temperatures below 560°C, the stable oxide is Fe_3O_4, which is formed according to the equation

$$3\mathrm{Fe} + 2\mathrm{O_2} = \mathrm{Fe_3O_4}. \tag{16}$$

The oxidation of chromium takes place according to

$$2\mathrm{Cr} + \frac{3}{2}\mathrm{O_2} = \mathrm{Cr_2O_3}. \tag{17}$$

The heat released during the oxidation is calculated as a weighed average of the heat released during the oxidation of Cr and Fe, i.e., $\Delta H_{ox} = 0.17\Delta H_{Cr_2O_3} + 0.83\Delta H_{FeO}$ at high temperatures. At low temperatures, we neglect oxidation since its rate is very small. Thus, the heat of reaction from the formation of Fe_3O_4 is not included in our calculations. The energies of reaction used are $\Delta H_{Cr_2O_3} = 4.5 \times 10^6$ J/kg and $\Delta H_{FeO} = 2.18 \times 10^6$ J/kg, calculated at 1400°C [14].

For the composite particles, the oxidation is considered for the matrix, which is composed of Ni and Cr. The oxidation of Cr takes place according to (17). The oxidation of Ni takes place according to

$$\mathrm{Ni} + \frac{1}{2}\mathrm{O_2} = \mathrm{NiO}. \tag{18}$$

The heat released during the oxidation is calculated as a weighed average of the heat released during the oxidation of Cr and Ni, i.e., $\Delta H_{ox} = \varepsilon_{Cr}\Delta H_{Cr_2O_3} + \varepsilon_{Ni}\Delta H_{NiO}$. The energies of reaction used are $\Delta H_{Cr_2O_3} = 4.3 \times 10^6$ J/kg, and $\Delta H_{NiO} = 1 \times 10^6$ J/kg, calculated at 1500°C [14].

4. Particle flight dynamics

The following particle equation of motion is used:

$$\frac{\mathrm{d}V_p}{\mathrm{d}t} = g\left[1 - \frac{\rho_g}{\rho_p}\right] + \frac{3}{8R}\frac{\rho_g}{\rho_p}|V_p - V_g|(V_p - V_g)C_d, \tag{19}$$

where C_d is calculated from [10]:

$$C_{drag} = \frac{24}{Re} + \frac{6}{1+\sqrt{Re}} + 0.4 \quad \text{for} \quad \leqslant 0 \leqslant Re \leqslant 2 \times 10^5 \tag{20}$$

while the particle position is calculated from

$$\frac{dX_p}{dt} = V_p. \tag{21}$$

The gas velocity V_g is obtained from experimental data [13]

$$V_g = V_{g0} + (V_{gp} - V_{g0}) z l^{-1}, \quad 0 \leqslant z \leqslant l, \tag{22}$$

$$V_g = (z_m - l)^{-1}\left[(V_{gm} - V_{gp})z + V_{gp} z_m - V_{gm} l\right], \quad l \leqslant z \leqslant z_m, \tag{23}$$

$$V_g = (z_c - z_m)^{-1}\left[(V_{gc} - V_{gm})z + V_{gm} z_c - V_{gc} z_m\right], \quad z_m \leqslant z \leqslant z_c, \tag{24}$$

$$V_g = (L - z_c)^{-1}\left[(V_{gs} - V_{gc})z + V_{gc} L - V_{gs} z_c\right], \quad z_c \leqslant z \leqslant L, \tag{25}$$

where $V_{g0} = 450$ m/s, $V_{gp} = 480$ m/s, $V_{gm} = 500$ m/s, $V_{gc} = 450$ m/s and $V_{gs} = 400$ m/s. The constants l, z_m, z_c and L are nozzle geometry dependent and are 0.1, 0.22, 0.4 and 0.6 m, respectively. The temperature is specified in a similar way with the constants: $T_{g0} = 2750$°C, $T_{gp} = 2600$°C, $T_{gm} = 2350$°C, $T_{gc} = 1000$°C and $T_{gs} = 500$°C.

5. Finite difference formulation

In order to develop a finite difference formulation for this system of equations, two issues stemming from Eq. (2) must be resolved. First, at the particle center ($r = 0$), the second term on the RHS becomes indeterminate. Using L'Hospital's rule, we get

$$\psi(T)\frac{\partial T}{\partial t} = 3\alpha \left.\frac{\partial^2 T}{\partial r^2}\right|_{r=0} \tag{26}$$

as the equation to be discretized at the particle center. Second, since $\psi(T)$ is multiplied by the derivative of T, the equation is nonlinear. Numerically, the equation is linearized by evaluating $\psi(T)$ at the previous time step. Using the Crank–Nicolson method, the finite difference formulation of Eq. (26) can be written as

$$(\psi_0^n + 3\alpha l) T_0^{n+1} - 3\alpha l T_1^{n+1} = (\psi_0^n - 3\alpha l) T_0^n + 3\alpha l T_1^n, \tag{27}$$

where $l = \Delta t/\Delta r^2$, superscript n is the time step index, subscript 0 is the position index corresponding to the mesh point at the particle center and subscript 1 is the position index for the mesh point next to the center. The finite difference formulation of Eq. (2) can be written as

$$\alpha l(i^{-1} - 1) T_{i-1}^{n+1} + (2\psi_i^n + 2\alpha l) T_i^{n+1} - \alpha l(i^{-1} + 1) T_{i+1}^{n+1} = \alpha l(1 - i^{-1}) T_{i-1}^n + (2\psi_i^n - 2\alpha l) T_i^n + \alpha l(i^{-1} + 1) T_{i+1}^n, \quad i = 1, 2, 3, \ldots, N-1, \tag{28}$$

where N is the number of spatial points. At the particle surface, the convective boundary condition (5) can be written as

$$-T_{N-1}^{n+1} + \left(1 + \frac{h\Delta r}{k_i^n}\right) T_N^{n+1} = \frac{h\Delta r}{k_i^n} T_g. \tag{29}$$

In the case of oxidation, the boundary condition (14) can be written as

$$-T_{N-1}^{n+1} + \left(1 + \frac{U^n \Delta r}{k_N^n}\right) T_N^{n+1} = \frac{\rho \Delta H_{ox} \Delta r}{k_N^n} \frac{d\delta^n}{dt} + \frac{U^n \Delta r}{k_N^n} T_g, \tag{30}$$

where U is the overall heat transfer coefficient, defined as

$$U^n = \frac{1}{(\delta^n/k_{ox}) + (1/h)}. \tag{31}$$

Eqs. (27)–(29) or (30) are solved simultaneously using the Tri-Diagonal Matrix Algorithm (TDMA). The particle equation of motion (19) is solved using a second order accurate Adams–Bashforth scheme.

6. Results

We consider the flight dynamics and oxidation of particles of five different sizes, namely 20, 30, 40, 60 and 80 μmm diameter. The initial conditions for the calculations are taken at the exit of the combustion chamber. The initial particle velocity varies according to size, as shown in Fig. 4. The particles are initially in the solid phase at 1300°C and subsequently melt, superheat and possibly re-solidify during flight. Although the initial particle temperature should depend on the particle size, the residence time of the powder particles in the combustion chamber decreases with the increase in particle size. Thus, the smaller particles, although subjected to more rapid heating, have less time to be heated. For this reason, it can be assumed that the temperatures of the particles at the exit of the combustion chamber are approximately the same and equal to 1300°C. The results for both the ceramic composite and stainless steel particles are qualitatively similar. The results presented correspond to the composite particles with a metal matrix composed of 25% Cr and 75% Ni, unless otherwise stated.

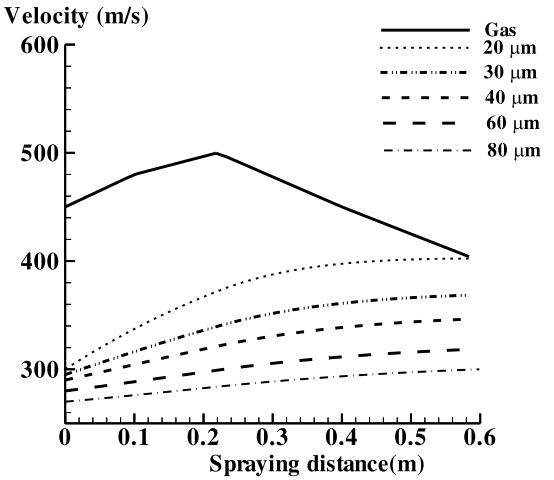

Fig. 4. Effect of particle size on the predicted particle velocity. The gas velocity is shown for reference.

7. In-flight dynamics and heat transfer

Fig. 4 shows the variation of the particle and gas velocities with spraying distance. Typical distances from the exit of the combustion chamber to the substrate are of the order of 30 cm, but could be as high as 60 cm. The initial particle and gas velocities were specified from experimental data. In Fig. 4 it is seen that the particle velocity increases with spraying distance. Also, it is seen that the smaller the particle, the smaller the relative velocity between the particle and the gas as expected from their small inertia. This is further reflected in the particle Reynolds number seen in Fig. 5, where it is clear that the particle Reynolds number is proportional to particle size. Also, the Reynolds number of the smallest particle approaches zero near the end of the simulation, since the particle and gas velocities approach each other as seen in Fig. 4. The change in the rate of increase of the particle Reynolds number after a spraying distance of 0.4 m is due to the change in the kinematic viscosity as a result of the change in gas temperature (see the experimental gas temperature shown in Fig. 10).

The variation of particle residence time with particle size is shown in Fig. 6. The figure shows that the time the particle takes to reach the substrate is proportional to its size. This is consistent with the velocity distribution seen in Fig. 4, where smaller particles have larger velocities. Fig. 7 shows the temporal development of the Cr_3C_2

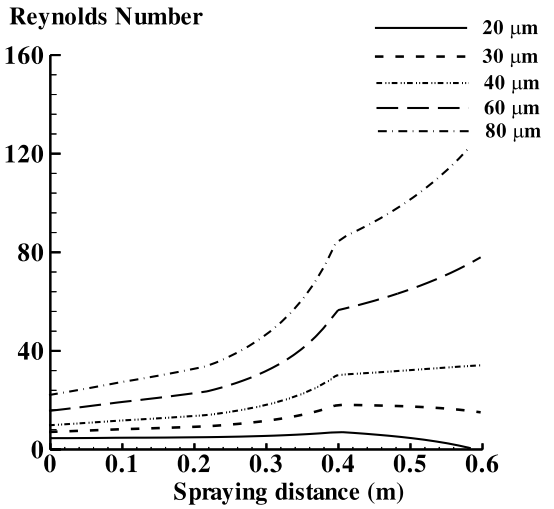

Fig. 5. Effect of particle size on the predicted particle Reynolds number.

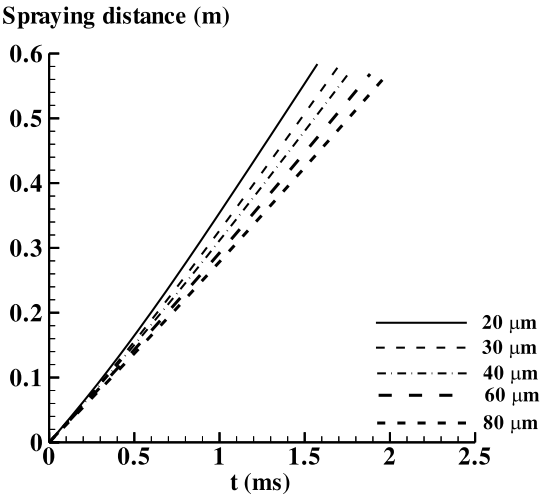

Fig. 6. Variation of the time taken to reach the substrate with particle size.

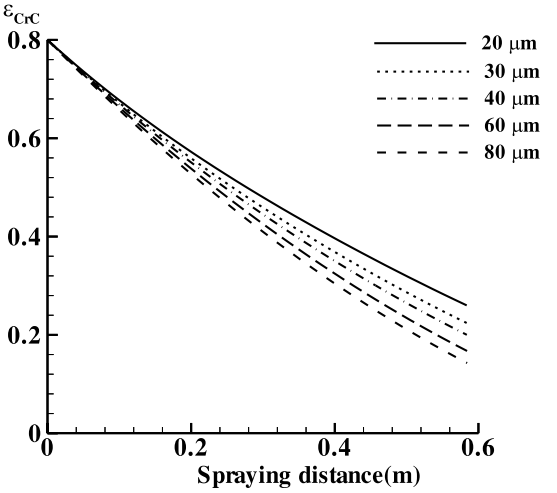

Fig. 7. Effect of particle size on the time development of the Cr_3C_2 volume fraction.

volume fraction (ε_{CrC}). The figure shows that larger particles undergo more dissolution than smaller ones due to the fact that they spend more time in-flight as seen in Fig. 6.

Fig. 8 shows the variation of the particle heat transfer coefficient with the spraying distance. The particle heat transfer coefficient is inversely proportional to the particle diameter since smaller particles have thinner thermal boundary layers around them. Also, it is seen that the heat transfer coefficient decreases with spraying distance as a direct consequence of the reduction of the gas thermal conductivity due to the decreasing gas temperature. The heat transfer coefficient of the smallest particle reaches a minimum near the end of the simulation, because the relative velocity between the particle and the gas reaches zero at that point (see the Reynolds number in Fig. 5).

Fig. 9 shows the surface temperature variation for the five particle sizes. The gas temperature is shown for reference. At the exit of the combustion chamber, the particles are solid powder at 1300°C. Because of their smaller thermal inertia, small particles melt quickly and acquire a higher maximum temperature than the larger particles. Also, due to the larger heat transfer coefficient of the small particles, they cool down faster and even partially solidify before reaching the substrate. On the other hand, larger particles (60 and 80 μm diameter), due to their large thermal inertia, do not completely melt (note that the liquidus temperature is 1440°C which is never reached by those two particles). On the other hand, all of the stainless steel particles in the 20–80 μm diameter range melt completely as seen in Fig. 10. The stainless steel has a lower liquidus temperature (1400°C). Our calculations show that the smallest stainless steel

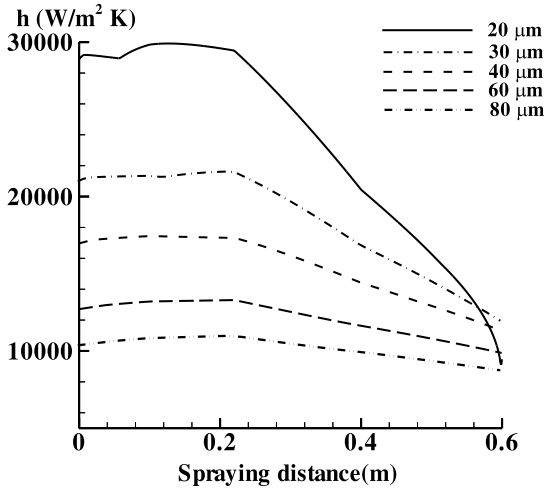

Fig. 8. Effect of particle size on the predicted convective heat transfer coefficient.

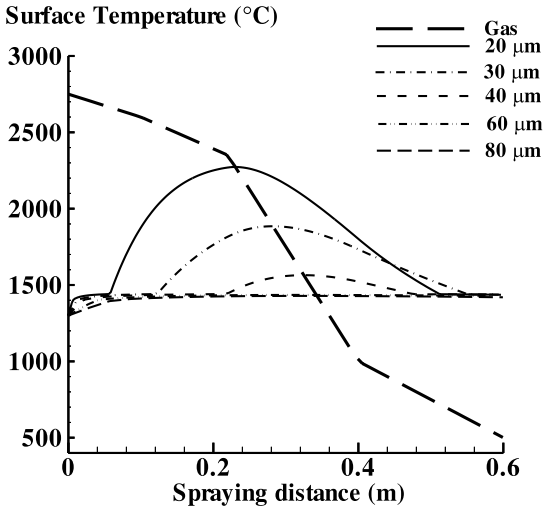

Fig. 9. Effect of particle size on the predicted particle surface temperature for the composite ceramic particles. Gas temperature is shown for reference.

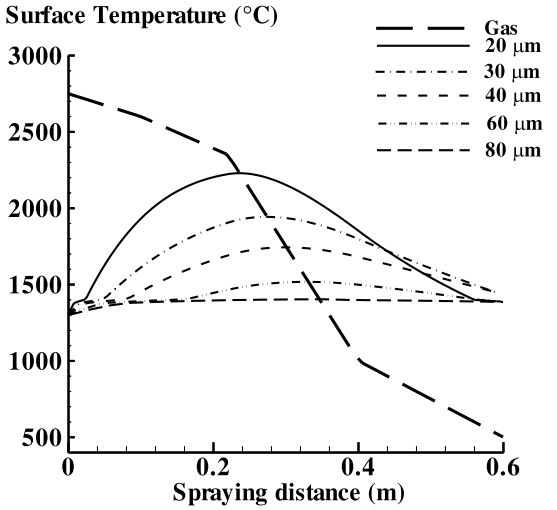

Fig. 10. Effect of particle size on the predicted particle surface temperature for stainless steel. Gas temperature is shown for reference.

particle (20 mm in diameter) takes about 0.082 ms, from the exit of the combustion chamber, to melt while the largest stainless steel particle (80 μm in diameter) takes about 1.18 ms to melt. In other words, increasing the stainless steel particle diameter four times, increases the melting time by 14-fold which is not far from the theoretical expectation which under identical surrounding conditions for both particles, would predict a characteristic melting time proportional to d^2. In order to show the effect of the powder composition, Fig. 11 shows the

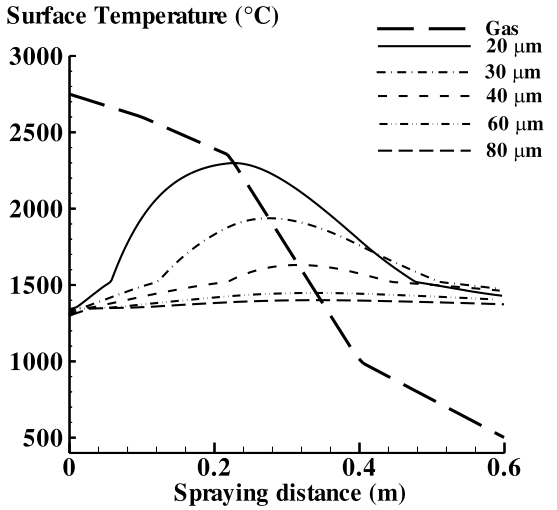

Fig. 11. Effect of particle size on the predicted particle surface temperature for a second composition with 75% Ni and 25% Cr. Gas temperature is shown for reference.

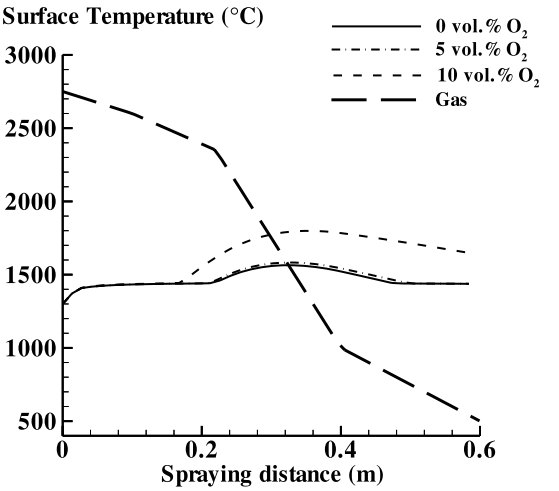

Fig. 12. Effect of oxygen volume fraction on the predicted particle surface temperature for the 40 μm diameter particle. Gas temperature is shown for reference.

surface temperature of composite particles that have a matrix composed of 35% Ni and 65% Cr. It is seen that the main difference between the two types of particles (Figs. 9 and 11) is the steeper temperature rise while the particle crosses the mushy region in the case with smaller Ni composition (Fig. 11). This is due to the higher liquidus temperature and the increased difference between the liquidus and solidus temperatures in this case.

8. Oxidation

Since in the HVOF spray process, the combustion products include oxygen, particle oxidation will invariably take place. In our calculations, we examined the effect of the presence of 5 vol% O_2 and 10 vol% O_2 in the combustion products for the five particle sizes studied in the previous section.

Fig. 12 shows the variation of the surface temperature of the 40 μm diameter particle with and without oxidation. The gas temperature is shown for reference. The figure shows that, the oxidation rate for the 5 vol% O_2 is much smaller than that for the 10 vol% O_2. This is reflected in the smaller change in particle surface temperature in the former compared to the latter. Similar results are found for other particles and hence are not shown here.

Figs. 13 and 14 show the time development of the oxidation layer thickness for the five particles for the 5 vol% O_2 and 10 vol% O_2, respectively. It is seen that, in both cases, the oxide thickness decreases with increasing particle diameter. This is due to the decrease in particle surface temperature with the diameter increase as seen in

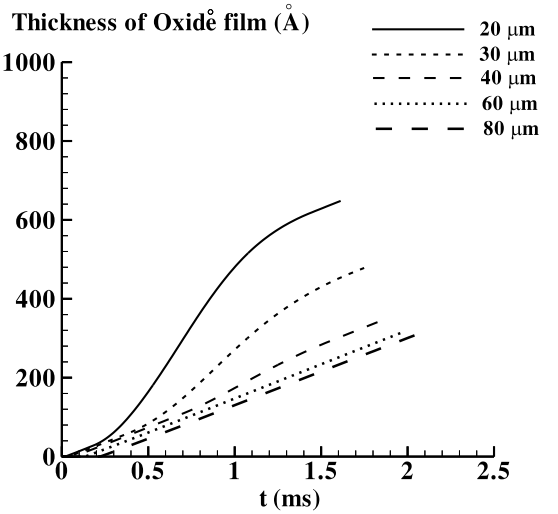

Fig. 13. Effect of particle size on the predicted oxide film thickness for the 5 vol% oxygen case.

Fig. 9. Because the oxidation has strong temperature dependence, smaller particles tend to oxide more since they attain higher temperatures. Also, the larger the particle, the longer the melting time, hence the later the oxidation can begin. By comparing Figs. 13 and 14, we see that the oxide layer thickness increases with the increase in the oxygen volume fraction as expected.

The temporal variation of the oxide volume fraction for the 10 vol% O_2 case for both stainless steel and the composite particle is shown in Fig. 15. The oxide volume fraction is inversely proportional to the particle diameter at all times. Also, the curves of the oxide volume frac-

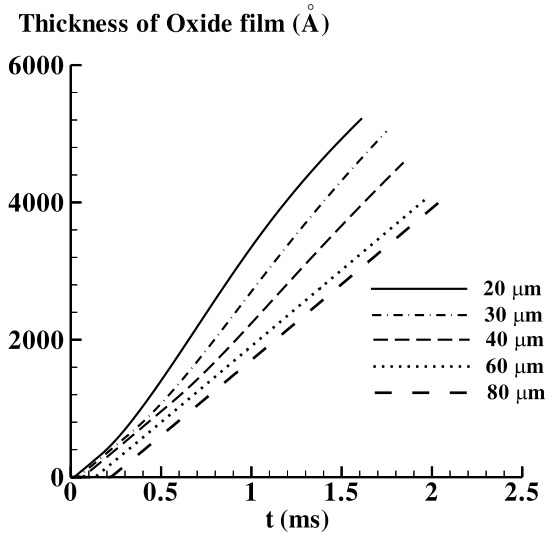

Fig. 14. Effect of particle size on the predicted oxide film thickness for the 10 vol% oxygen case.

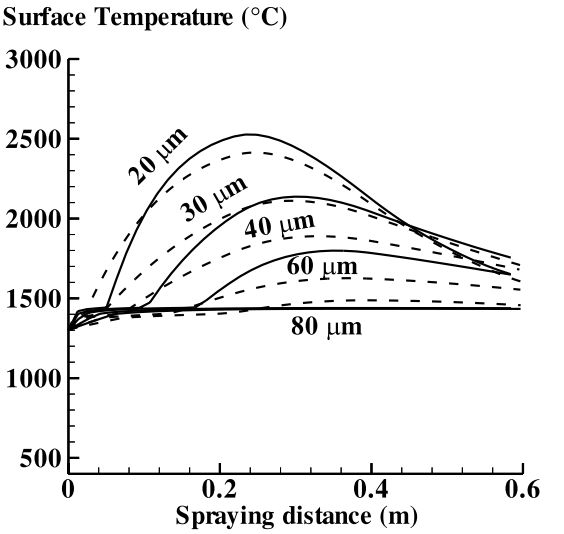

Fig. 16. Variation of the surface temperature with particle size. Solid lines (composite particles), dashed line (stainless steel particles).

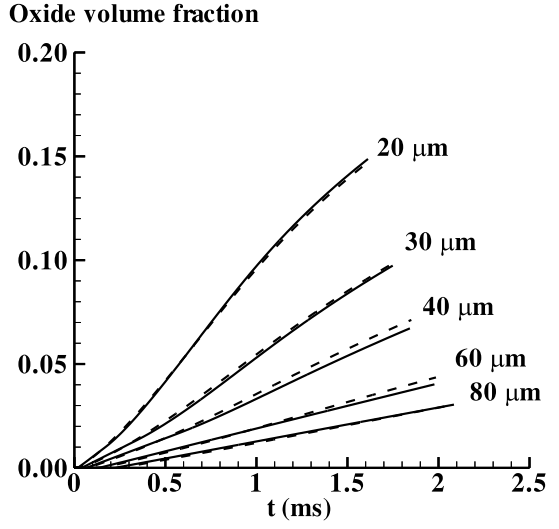

Fig. 15. Variation of oxide volume fraction with particle size for the case of 10 vol% oxygen. Solid lines (composite particles), dashed line (stainless steel particles).

tion for the stainless steel and composite particles tend to overlap. In order to explain this trend, we show in Fig. 16 the surface temperature for both stainless steel and the composite particles. This figure illustrates the relationship between the particle surface temperature and the size of the oxide layer formed, i.e. the higher the surface temperature the larger the size of the oxide layer.

To illustrate the capability of the model in a qualitative manner, Fig. 17 shows a micrograph of ceramic composite particles at approximately 20 vol% O_2 that shows that the oxide stringers have a thickness in the range of 0.7–1.5 μm in the deposit. It is to be emphasized however, that measurement of oxide thickness in the deposit can only provide an order-of-magnitude estimate of the in-flight oxidation, as, upon impact, oxide layers are subject to flattening, fracturing and even accumulation.

9. Conclusions

A mathematical model for the prediction of the in-flight oxidation of stainless steel and composite spherical particles during thermal spraying deposition has been developed. Available experimental data on stainless steel oxidation have been used to determine finite-rate oxidation equation constants. The model is capable of predicting the mechanical and thermal properties of the particles as well as the interrelation of the process parameters and the oxidation phenomenon. Of particular importance is the ability to predict the particle residence time, time of its melting and the conditions of the particle at the time of reaching the substrate.

The results show that smallest particles can reach the substrate completely solidified, while large particles can reach the substrate partially liquefied. Thus, the spraying distance should be carefully adjusted for optimum results. The oxide solid fraction is inversely proportional to the particle diameter and directly proportional to the particle surface temperature.

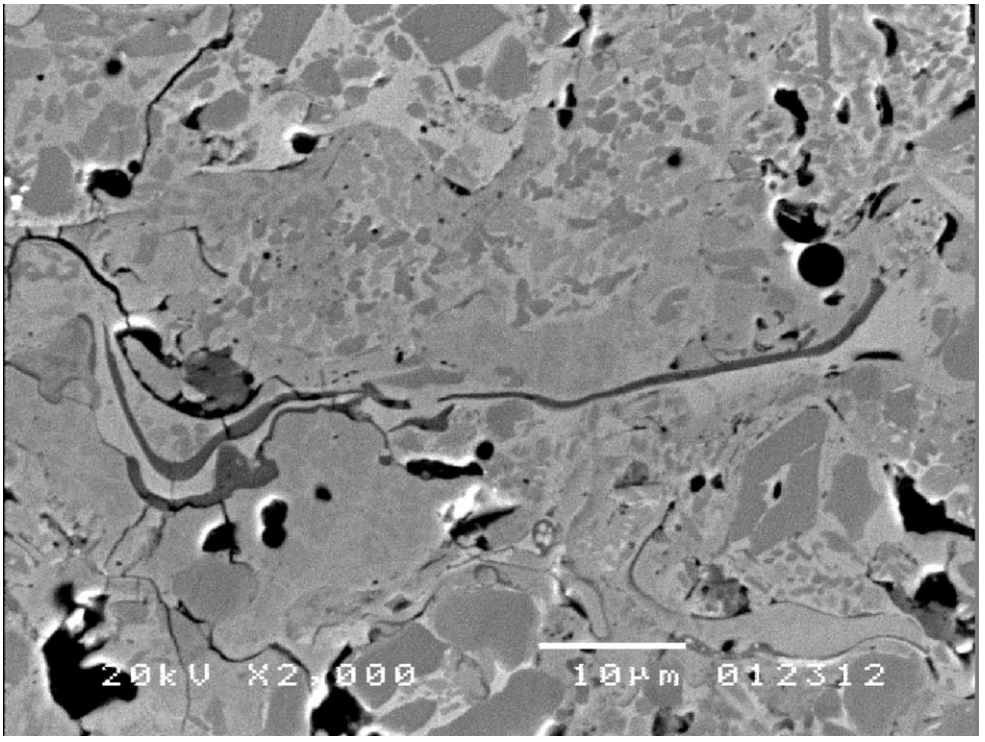

Fig. 17. A micrograph showing oxidation of deposited composite ceramic particles. The oxide layers are the thin gray stripes.

Acknowledgements

RHR acknowledges the Catalan Government for a visiting professorship at the University of Barcelona in the springs of 1999 and 2000. This work was supported in part by the Generalitat de Catalunya (project SGR99-51), CICYT (project MAT96-0426), NSF (CTS-9614653), and a Los Alamos National Laboratory (CULAR) grant.

References

[1] A.J Sturgeon, High velocity oxyfuel spraying promises better coatings, Met. Mater. 8 (1992) 547–548.
[2] V.V. Sobolev, J.M. Guilemany, Dynamic processes during high velocity oxyfuel spraying, Int. Mater. Rev. 41 (1996) 13–32.
[3] H.M. McCullough, M.G. Fontana, F.H. Beck, Formation of oxides on some stainless steels at high temperatures, Trans. Amer. Soc. Metals 43 (1951) 404–425.
[4] J.C. Colson, J.P. Larpin, High-temperature oxidation of stainless steels, MRS Bull. (1994) 23–25.
[5] S.L. Dai, J.-P. Delplanque, E.J. Lavernia, Microstructural characteristics of 5083 Al alloys processed by reactive spray deposition for net-shape manufacturing, Metal. Mater. Trans. A 29 (1998) 2597–2611.
[6] J.-P. Delplanque, E.J. Lavernia, R.H. Rangel, Analysis of inflight oxidation during reactive spray atomization and deposition processing of aluminum, J. Heat Transfer 122 (2000) 126–133.
[7] M.C. Flemings, Solidification Processing, McGraw-Hill, New York, NY, 1974.
[8] W.E. Ranz, W.R. Marshall, Evaporation from drops (Part I), Chem. Eng. Prog. 48 (3) (1952) 141–180.
[9] Y.C. Lee, Y.P. Chyou, E. Pfender, Particle dynamics and particle heat and mass transfer in thermal plasmas. Part II. Particle heat and mass transfer in thermal plasmas, Plasma Chem. Plasma Process. 5 (4) (1985) 391–414.
[10] F.M. White, Viscous Fluid Flow, McGraw-Hill, New York, NY, 1974.
[11] V.V. Sobolev, J.M. Guilemany, J.A. Calero, Dynamic processes during in-flight motion of Cr_3C_2–NiCr powder particles in HVOF spraying, J. Mater. Process. Manuf. Sci. 4 (1996) 25–39.
[12] F.P. Fehlner, Low-temperature Oxidation: The Role of Vitreous Oxides, Wiley, New York, 1986.
[13] A.J. Martin, Caracterización de recubrimientos de acero inoxidable obtenidos mediante proyección térmica, Doctoral Thesis, University de Barcelona, 1999.
[14] L.S. Darken, R.W. Gurry, Physical Chemistry of Metals, McGraw-Hill, New York, NY, 1953.